Comput Mech (2010) 46:31–41
DOI 10.1007/s00466-009-0425-0

ORIGINAL PAPER

Wall shear stress calculations in space–time finite element computation of arterial fluid–structure interactions

Kenji Takizawa · Creighton Moorman · Samuel Wright · Jason Christopher · Tayfun E. Tezduyar

Received: 6 September 2009 / Accepted: 24 September 2009 / Published online: 10 October 2009

Abstract The stabilized space–time fluid–structure interaction (SSTFSI) technique was applied to arterial FSI problems soon after its development by the Team for Advanced Flow Simulation and Modeling. The SSTFSI technique is based on the Deforming-Spatial-Domain/Stabilized Space–Time (DSD/SST) formulation and is supplemented with a number of special techniques developed for arterial FSI. The special techniques developed in the recent past include a recipe for pre-FSI computations that improve the convergence of the FSI computations, using an estimated zero-pressure arterial geometry, Sequentially Coupled Arterial FSI technique, using layers of refined fluid mechanics mesh near the arterial walls, and a special mapping technique for specifying the velocity profile at inflow boundaries with non-circular shape. In this paper we introduce some additional special techniques, related to the projection of fluid–structure interface stresses, calculation of the wall shear stress (WSS), and calculation of the oscillatory shear index. In the test computations reported here, we focus on WSS calculations in FSI modeling of a patient-specific middle cerebral artery segment with aneurysm. Two different structural mechanics meshes and three different fluid mechanics meshes are tested to investigate the influence of mesh refinement on the WSS calculations.

Keywords Cardiovascular fluid mechanics · Cerebral aneurysms · Patient-specific data · Fluid–structure interactions · Hyperelastic material · Space–time methods · Wall shear stress · Oscillatory shear index

K. Takizawa · C. Moorman · S. Wright · J. Christopher ·
T. E. Tezduyar (✉)
Mechanical Engineering, Rice University-MS321,
6100 Main Street, Houston, TX 77005, USA
e-mail: tezduyar@rice.edu

1 Introduction

We have seen much emphasis in recent years on arterial fluid–structure interaction (FSI) computations (see, for example [1–18]). We have also often seen discussion of wall shear stress (WSS) distribution on the arterial walls. Since WSS is a rather sensitive quantity, deformation of the arterial walls, which is taken into account in FSI modeling, plays an important role in WSS calculations. This was pointed out in a number of articles, including [1,3,12]. For examples of method development for FSI modeling in general, see [19–47]. The Deforming-Spatial-Domain/Stabilized Space–Time (DSD/SST) formulation [48–51] was introduced as a general-purpose interface-tracking (moving-mesh) technique for flows with moving boundaries and interfaces, including FSI. The stabilization components used are the Streamline-Upwind/Petrov–Galerkin (SUPG) [52,53] and Pressure-Stabilizing/Petrov–Galerkin (PSPG) [48,54] methods. An earlier version of the pressure stabilization, for Stokes flows, was introduced in [55]. The DSD/SST formulation, together with the mesh update methods [56–58] developed in conjunction with the DSD/SST formulation and block-iterative coupling [59] (see [34,35,45] for the terminology), has been the core technology used in the arterial FSI computations reported by Torii et al. [1,3,4,6,8,11,14,18] for patient-specific image-based geometries. The cases studied in these articles by Torii et al. were almost all for middle cerebral artery segments with aneurysm, and the geometries were constructed from computed tomography images.

The stabilized space–time FSI (SSTFSI) technique was introduced in [45]. It is based on the new-generation DSD/SST formulations, which were also introduced in [45], and was slightly modified in [16] for better incompressibility constraint representation. The SSTFSI technique was extended in [7,9,13,16,17] to arterial FSI, with emphasis on arteries with aneurysm. The arterial geometries used in [7,9,13] were approximations to patient-specific image-based geometries, mainly to one of the geometries reported by Torii et al., which was also used in [16,17] without approximation. A number of special techniques for arterial FSI computations were developed in conjunction with the SSTFSI technique. The special techniques developed in the recent past include a recipe for pre-FSI computations that improve the convergence of the FSI computations [7,9], using an estimated zero-pressure arterial geometry [9,16,17,60], Sequentially-Coupled Arterial FSI technique [9,13,17,61], a special mapping technique for specifying the velocity profile at inflow boundaries with non-circular shape [16,17], and using layers of fluid mechanics mesh refined in the normal direction near the arterial walls [13,16,17]. With the explicitly controlled mesh refinement in the normal direction near the arterial wall and on the wall, we can increase the accuracy in computing the WSS. Computations with refinement in the normal direction were reported in [16,17]. In this paper we present computations with fluid mechanics meshes refined also on the wall. In this paper, we also introduce some additional special techniques, related to the projection of fluid–structure interface stresses, calculation of the WSS, and calculation of the oscillatory shear index (OSI). In the test computations reported here, we use actual patient-specific image-based data. Specifically, we focus on the bifurcating middle cerebral artery segment of a 67 year-old female with aneurysm, which was reported in [8,11,14]. The structural modeling for the arteries is based on the continuum element made of hyperelastic (Fung) material.

For the governing equations and the SSTFSI technique, we refer the reader to [7,9,16,17,45]. Projection of fluid–structure interface stresses, calculation of the WSS, and calculation of the oscillatory shear index are described in Sect. 2. General conditions for the test computations are given in Sect. 3, and the test results are presented in Sect. 4. The concluding remarks are given in Sect. 5.

2 Special techniques

2.1 Stress projection

In the SSTFSI technique proposed in [45], the fluid stresses are projected to the fluid–structure interface by using the following equation:

$$\int_{(P_n)_h} (\mathbf{w}^h_{1\mathrm{I}})^-_{n+1} \cdot \mathbf{h}^h_{1\mathrm{I}} dP = -\int_{(P_n)_h} (\mathbf{w}^h_{1\mathrm{I}})^-_{n+1} \cdot p^h \mathbf{n} dP + \int_{Q_n} 2\mu\boldsymbol{\varepsilon}((\mathbf{w}^h_{1\mathrm{I}})^-_{n+1}) : \boldsymbol{\varepsilon}(\mathbf{u})\, dQ + \int_{Q_n} (\mathbf{w}^h_{1\mathrm{I}})^-_{n+1} \cdot \boldsymbol{\nabla} \cdot (2\mu\boldsymbol{\varepsilon}(\mathbf{u}))\; dQ. \tag{1}$$

Here, $\mathbf{u}$, p, μ and $\boldsymbol{\varepsilon}(\mathbf{u})$ are the velocity, pressure, viscosity and strain-rate tensor, where $\boldsymbol{\varepsilon}(\mathbf{u}) = \left((\boldsymbol{\nabla}\mathbf{u}) + (\boldsymbol{\nabla}\mathbf{u})^T\right)/2$. The symbol Q_n represents the slice of the space–time domain between the time levels t_n and t_{n+1} (the space–time volume between the spatial domains Ω_n and Ω_{n+1}), P_n is the lateral boundary of Q_n, and $\mathbf{n}$ is the unit outward normal vector at the boundary Γ of the domain Ω. The subscripts "1" and "I" represent the fluid and the interface, $\mathbf{h}^h_{1\mathrm{I}}$ is the fluid stress at the interface, and $\mathbf{w}^h$ is the finite element test function. The notations $(\cdot)^-_n$ and $(\cdot)^+_n$ denote the function values at t_n as approached from below and above.

The SSTFSI technique has two more projection equations at the fluid–structure interface—one from the structural displacement rate to the fluid velocity $(\mathbf{u}^h_{1\mathrm{I}})^-_{n+1}$, and the other from the fluid stresses to the structural stresses. Although this detail was not described in [45], these two projection equations are solved by "numerical substitution", which essentially consists of sub-level GMRES [62] iterations. If the fluid and structure meshes at the interface are compatible, the two projections simplify to copying operations.

In the "Separated Stress Projection (SSP)" option proposed in [63], the pressure and viscous parts of $\mathbf{h}^h_{1\mathrm{I}}$ are projected to the structure interface separately, pressure as a scalar and viscous stress as a vector. They are then combined as $-p^h_{2\mathrm{I}}\mathbf{n} + \left(\mathbf{h}^h_v\right)_{2\mathrm{I}}$ while integrating the interface stresses in the structural mechanics equations. Here the subscript "2" refers to the structure, $\mathbf{n}$ is the unit normal vector at the integration point, and $p^h_{2\mathrm{I}}$ and $\left(\mathbf{h}^h_v\right)_{2\mathrm{I}}$ are the interpolated values at the integration point.

The pressure projection equation can also be solved by numerical substitution and would simplify to a copying operation if the fluid and structure meshes at the interface are compatible. The viscous part of the fluid interface stress, $(\mathbf{h}^h_v)_{1\mathrm{I}}$, is calculated as follows:

$$\int_{(P_n)_h} (\mathbf{w}^h_{1\mathrm{I}})^-_{n+1} \cdot (\mathbf{h}^h_v)_{1\mathrm{I}}\, dP = \int_{Q_n} 2\mu\boldsymbol{\varepsilon}((\mathbf{w}^h_{1\mathrm{I}})^-_{n+1}) : \boldsymbol{\varepsilon}(\mathbf{u}) dQ + \int_{Q_n} (\mathbf{w}^h_{1\mathrm{I}})^-_{n+1} \cdot \boldsymbol{\nabla} \cdot (2\mu\boldsymbol{\varepsilon}(\mathbf{u}))\, dQ. \tag{2}$$

We propose to lump the "mass" matrix associated with the first term in Eq. (2), and this becomes equivalent to a "direct substitution", which makes the computations more efficient.

Remark 1 We observe a smoother stress distribution with a lumped mass matrix than with a consistent mass matrix.

Remark 2 For the computations reported in this paper, we reconstruct the fluid interface stress vector from its pressure and viscous parts before projecting it to the structure. In that sense, the approach we use here does not have all the ingredients of the SSP technique, but the SSP ingredients we have are still helpful in increasing our accuracy and efficiency.

2.2 Wall shear stress calculation

We also propose a new technique for calculating the WSS. For that, we first decompose the spatial version of $(\mathbf{w}^h_{1\mathrm{I}})^-_{n+1}$ into its two components:

$$\mathbf{w}^h_{1\mathrm{I}} = (\mathbf{w}^h_{1\mathrm{I}})^{\mathrm{W}} + (\mathbf{w}^h_{1\mathrm{I}})^{\mathrm{R}}, \tag{3}$$

where $(\mathbf{w}^h_{1\mathrm{I}})^{\mathrm{R}}$ is the part associated with the rim nodes at the lumen ends, and $(\mathbf{w}^h_{1\mathrm{I}})^{\mathrm{W}}$ is the part associated with the rest of the fluid mechanics nodes at the arterial wall. We then calculate $(\mathbf{h}^h_v)_{1\mathrm{I}}$ as follows:

$$\int_{\Gamma_h} (\mathbf{w}^h_{1\mathrm{I}})^{\mathrm{W}} \cdot (\mathbf{h}^h_v)_{1\mathrm{I}}\, d\Gamma = \int_{\Omega} 2\mu\boldsymbol{\varepsilon}((\mathbf{w}^h_{1\mathrm{I}})^{\mathrm{W}}) : \boldsymbol{\varepsilon}(\mathbf{u})\, d\Omega + \int_{\Omega} (\mathbf{w}^h_{1\mathrm{I}})^{\mathrm{W}} \cdot \boldsymbol{\nabla}\cdot(2\mu\boldsymbol{\varepsilon}(\mathbf{u}))\; d\Omega, \tag{4}$$

$$\int_{\Gamma_h} (\mathbf{w}^h_{1\mathrm{I}})^{\mathrm{R}} \cdot \left(\left(\mathbf{n}\times\mathbf{e}^{\mathrm{R}}\right)\cdot\boldsymbol{\nabla}\right)(\mathbf{h}^h_v)_{1\mathrm{I}}\, d\Gamma = 0, \tag{5}$$

where $\mathbf{e}^{\mathrm{R}}$ is the unit vector along the rim.

2.3 Oscillatory shear index

The OSI is a measure of the degree to which WSS oscillates during a heart beat cycle. It is defined (see [64]) as follows:

$$\mathrm{OSI} = \frac{1}{2}\left(1 - \frac{(\mathbf{h}^h_v)^{\mathrm{NM}}_{1\mathrm{I}}}{(\mathbf{h}^h_v)^{\mathrm{MN}}_{1\mathrm{I}}}\right), \tag{6}$$

where “NM” and “MN” stand for “norm of the mean” and “mean of the norm”, and

$$(\mathbf{h}^h_v)^{\mathrm{NM}}_{1\mathrm{I}} = \frac{1}{T}\left\|\int_0^T (\mathbf{h}^h_v)_{1\mathrm{I}} dt\right\|, \tag{7}$$

$$(\mathbf{h}^h_v)^{\mathrm{MN}}_{1\mathrm{I}} = \frac{1}{T}\int_0^T \left\|(\mathbf{h}^h_v)_{1\mathrm{I}}\right\| dt. \tag{8}$$

Here T is the period of the cardiac cycle. Higher OSI indicates larger flow direction variation in a cardiac cycle. Calculating the OSI based on a fixed reference frame is not the best way, because, for example, if an artery segment undergoes rigid-body rotation, that should not influence the OSI. Therefore we want to exclude rigid-body rotation from the calculation. We propose two methods for the OSI calculation.

Method 1

$$(\mathbf{h}^h_v)^{\triangle}_{1\mathrm{I}} = J\mathbf{F}^{-1}(\mathbf{h}^h_v)_{1\mathrm{I}}, \tag{9}$$

where $\mathbf{F}$ is the deformation gradient tensor associated with the deformation of the fluid–structure interface (not the volumetric deformation gradient of the fluid-domain motion), and $J = det\mathbf{F}$.

Method 2

$$(\mathbf{h}^h_v)^{\triangle}_{1\mathrm{I}} = \mathbf{R}^T(\mathbf{h}^h_v)_{1\mathrm{I}}, \tag{10}$$

where $\mathbf{R}$ is the rotation tensor coming from the decomposition of $\mathbf{F}$ as

$$\mathbf{F} = \mathbf{R}\mathbf{U}, \tag{11}$$

and $\mathbf{U}$ is the right stretch tensor.

For both methods, we calculate $(\mathbf{h}^h_v)^{\triangle}_{1\mathrm{I}}$ as follows:

$$\int_{(\Gamma_{1\mathrm{I}})_{\mathrm{REF}}} \mathbf{w}^h_{1\mathrm{I}} \cdot (\mathbf{h}^h_v)^{\triangle}_{1\mathrm{I}} d\Gamma = \int_{(\Gamma_{1\mathrm{I}})_{\mathrm{REF}}} \mathbf{w}^h_{1\mathrm{I}} \cdot \mathcal{R}(\mathbf{h}^h_v)_{1\mathrm{I}} d\Gamma, \tag{12}$$

where $\mathcal{R} = J\mathbf{F}^{-1}$ or $\mathcal{R} = \mathbf{R}^T$, and $(\Gamma_{1\mathrm{I}})_{\mathrm{REF}}$ is a reference configuration of the fluid–structure interface. With this, in Eqs. (7) and (8), we replace $(\mathbf{h}^h_v)_{1\mathrm{I}}$ with the $(\mathbf{h}^h_v)^{\triangle}_{1\mathrm{I}}$.

Remark 3 A similar concept can be found in [65] as the corotated Cauchy stress, $\mathbf{R}^T\boldsymbol{\sigma}\mathbf{R}$, where $\boldsymbol{\sigma}$ is the Cauchy stress tensor.

Remark 4 We used Eq. (9) for the WSS calculations reported in this paper.

Remark 5 A reference configuration is not necessarily the unstressed configuration of the fluid–structure interface. For the calculations reported in this paper, it is the configuration corresponding to the instant when the pressure is at its time-averaged value (on the way up, i.e. at the ascending part of the pressure curve).

3 General conditions for the test computations

For integration of the incompressibility-constraint term over each space–time slab, we use only one integration point in time, shifted to the upper time level of the slab (see [16]). At inflow boundaries with non-circular shape, we use a special mapping technique [16] for specifying the velocity profile, which is obtained by mapping from a preferred inflow profile given over a circular cross-section. All computations were carried out in a parallel computing environment and were completed without any remeshing. The fully-discretized, coupled fluid and structural mechanics and mesh-moving equations are solved with the quasi-direct coupling technique (see Section 5.2 in [45]). In solving the linear equation systems involved at every nonlinear iteration, the GMRES search technique [62] is used with a diagonal preconditioner. The S → F → S → FSI sequence is used in the computations (see Section 6.2 in [9] for the terminology). This is slightly different from the S → F → FSI sequence described in [9] in that it includes an extra structural mechanics step which incorporates traction obtained from the fluid computation. This helps match the structure mesh to the fluid solution and provides a better starting point for FSI computations.

3.1 Fluid and structure properties

As it was done for the computations reported in [1,3,4,6,8], the blood is assumed to behave like a Newtonian fluid (see Section 2.1 in [9]). The density and kinematic viscosity are set to 1,000 kg/m^3 and 4.0×10^{-6} m^2/s. The material density of the arterial wall is known to be close to that of the blood and therefore set to 1,000 kg/m^3. The arterial wall is modeled with the continuum element made of hyperelastic (Fung) material. The Fung material constants D_1 and D_2 (from [66]) are 2.6447×10^3 N/m^2 and 8.365, and the penalty Poisson's ratio is 0.45. Cerebral arteries are surrounded by cerebrospinal fluid, and we expect that to have a damping effect on the structural dynamics of the arteries. Therefore we add a mass-proportional damping, which also helps in removing the high-frequency modes of the structural deformation. The damping coefficient η is chosen in such a way that the structural mechanics computations remain stable at the time-step size used. The value of η used in the test computations reported in this paper will be given in the section where we describe those test computations.

3.2 Boundary conditions

At the inflow boundary we specify the velocity profile as a function of time, by using the special mapping technique mentioned above, and based on a velocity waveform which represents the cross-sectional maximum velocity as a function of time. For details, see [16]. Figure 1 shows the volumetric flow rate. At the outflow boundaries, we specify the same traction boundary condition. The traction condition is based on a pressure profile, which, as a function of time, is determined based on the flow rate using the Windkessel model [67]. The pressure profile range is from 80 to 120 mm Hg (normal blood pressure range). For details, see [16]. Figure 2 shows the pressure profile as a function of time. On the arterial walls, we specify no-slip boundary conditions for the

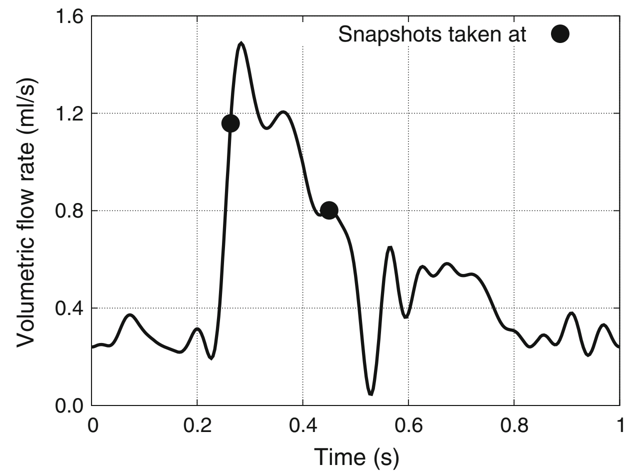

Fig. 1 Volumetric flow rate, with marks where the snapshots shown in Fig. 13 were taken

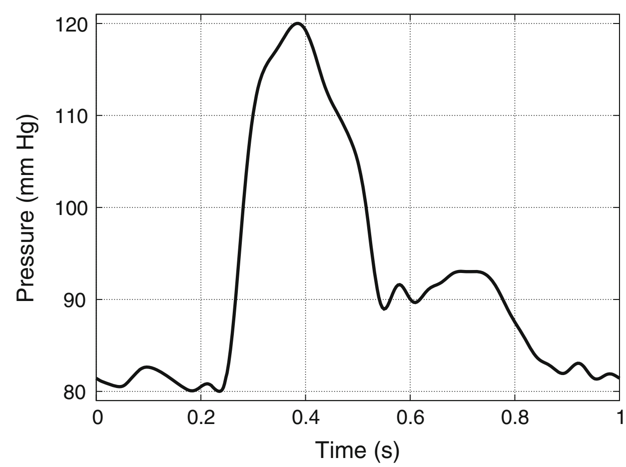

Fig. 2 Outflow pressure profile

flow. In the structural mechanics part, as a boundary condition at the ends of the arteries, we set the normal component of the displacement to zero, and for one of those nodes we also set to zero the tangential displacement component that needs to be specified to preclude rigid-body motion.

3.3 Preconditioning technique

In computations with hyperelastic materials, we do not compute the diagonal of the tangent stiffness matrix. Therefore, as proposed in [13], we use a diagonal preconditioner based on the assembly of only the element-level lumped mass matrices $\mathbf{m}^e_{\text{LUMP}}$, but after being multiplied by a factor that, to some extent, takes into account the material stiffness. The expression for that multiplication factor can be found in [13]. We use the "Selective Scaling" technique (see Remark 14 in [45]) to dynamically shift the emphasis between the fluid and structure parts.

4 Test computations

4.1 Geometry and arterial wall

The geometry of the arterial lumen is from [8,11,14], which was extracted from the computed tomography model of a bifurcating segment of the middle cerebral artery of a 67-year-old female with aneurysm. The diameter of the arterial lumen is 2.39 mm at the inflow, and 1.53 and 1.73 mm at the two outflow ends. The Womersley parameter (defined in [16]) and the period of the cardiac cycle are 1.5 and 1.0 s, respectively. We use the "estimated zero-pressure arterial geometry", as described in [9,60]. In estimating that geometry, the time-averaged value of the blood pressure, obtained by averaging over a cardiac cycle, is 92.2 mm Hg. As the zero-pressure shape, we use a scaled down version of the geometry used in [8,11,14]. We try different wall-thickness ratios with the zero-pressure shape until we obtain, approximately, a 10% wall-thickness ratio (relative to the diameter of the arterial lumen) at the inflow. At each iteration, the trial wall-thickness ratio is globally uniform, but the base length scales for the four "patches" are defined individually, with a smooth transition between the patches. The length scales for the inflow and two outflow patches are the lumen diameters at those ends. The length scale for the aneurysm patch is 0.67× (lumen diameter at the inflow). The details of this technique can be found in [16]. A simple, general technique for wall-thickness prescription, based on the solution of the Laplace's equation, was developed in [68].

4.2 Structural mechanics meshes

Two structural mechanics meshes are used. The coarse structure mesh consists of 8,067 nodes and 5,316 eight-node hexahedral elements, with 2,689 nodes and 2,658 four-node quadrilateral elements on the fluid–structure interface. Meanwhile, the fine structure mesh consists of 30,732 nodes and 20,366 eight-node hexahedral elements, with 10,244 nodes and 10,183 four-node quadrilateral elements on the fluid–structure interface. Figure 3 shows the structural mechanics meshes. For both structural mechanics meshes we have two layers of elements across the arterial wall, which we believe to be sufficient based on our earlier numerical tests involving the inflation of a thick-walled cylinder slice. Those tests were carried out with 3D elements, under plane-strain conditions, and with material properties and length and force scales similar to those we are using for the arterial wall. The results were accurate even with a single element across the arterial wall. In addition, we reported in [16] tests we carried out with the actual arterial geometry and with 1, 2 and 4 elements across the arterial wall. The tests showed that the results for all hexahedral meshes were geometrically almost identical during the cardiac cycle. A quantitative comparison based on the lumen volumes also showed that the results obtained with different numbers of elements across the arterial wall were very close. Figure 3 also serves the purpose of comparing, when the outflow pressure is maximum, the deformations obtained with the coarse and fine structural mechanics meshes (with the fine fluid mechanics mesh described in the next subsection). The main discrepancy between the results is the position of the outlets. The refined structural mechanics mesh is used in generating a fine fluid interface mesh, which in turn is used in generating the "fine" fluid mechanics volume mesh (see next subsection).

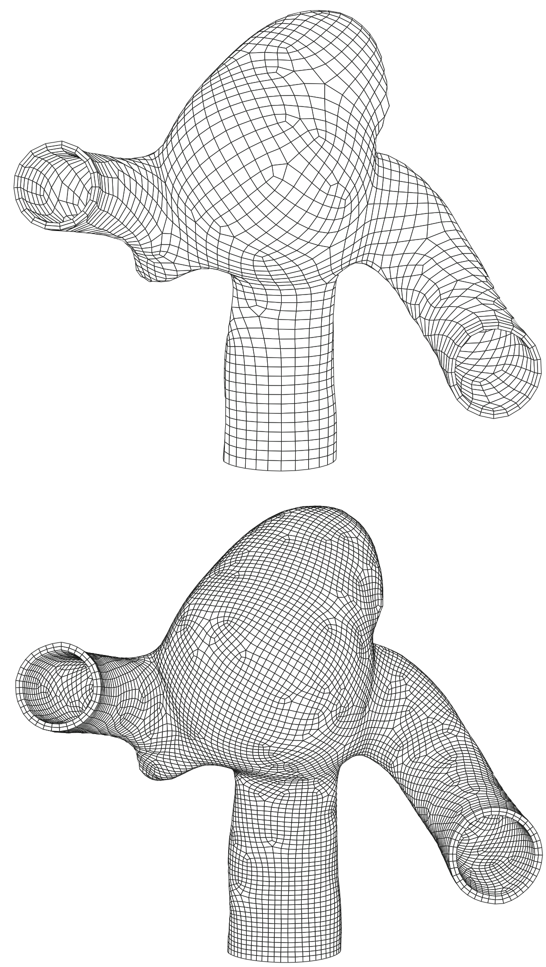

Fig. 3 A bifurcating middle cerebral artery segment with aneurysm. Coarse (*top*) and fine (*bottom*) structural mechanics meshes when the outflow pressure is maximum

4.3 Fluid mechanics meshes

We use three different fluid mechanics meshes: a "coarse" mesh with 15,850 nodes and 88,573 four-node tetrahedral elements, a "medium" mesh with 22,775 nodes and 128,813 four-node tetrahedral elements, and a "fine" mesh with 138,713 nodes and 823,756 four-node tetrahedral elements. The medium and fine meshes have four boundary layer

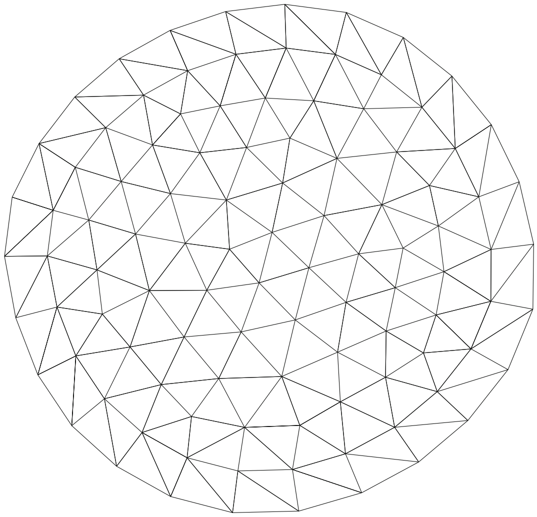

Fig. 4 A bifurcating middle cerebral artery segment with aneurysm. Inflow plane for the coarse fluid mechanics mesh

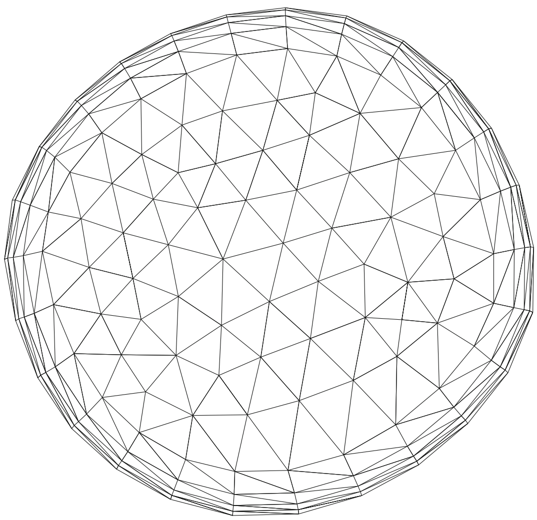

Fig. 5 A bifurcating middle cerebral artery segment with aneurysm. Inflow plane for the medium fluid mechanics mesh

elements. The thickness of the first layer for both meshes is approximately 0.02 mm. The coarse mesh has one layer of elements with a uniform thickness of approximately 0.2 mm. Figures 4, 5 and 6 show the inflow plane for the coarse, medium and fine meshes. The coarse and medium meshes have the same number of nodes and elements at the fluid–structure interface: 3,057 nodes and 6,052 three-node triangular elements, and that is shown in Fig. 7. The fluid–structure interface mesh for the fine mesh has 11,713 nodes and 23,304 three-node triangular elements and is shown in Fig. 8.

4.4 Other computational parameters and conditions

The computations are carried out with the SSTFSI-TIP1 technique (see Remarks 4 and 7 in [9]) and the SUPG test

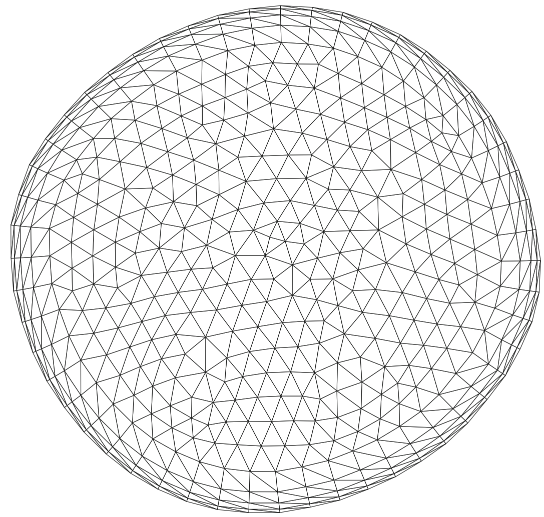

Fig. 6 A bifurcating middle cerebral artery segment with aneurysm. Inflow plane for the fine fluid mechanics mesh

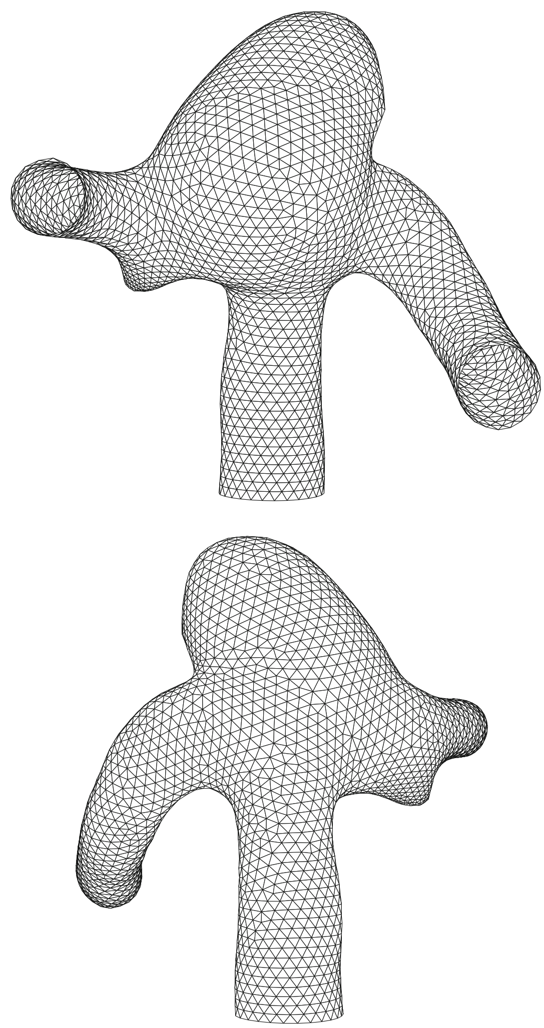

Fig. 7 A bifurcating middle cerebral artery segment with aneurysm. Fluid–structure interface for the coarse and medium fluid mechanics meshes

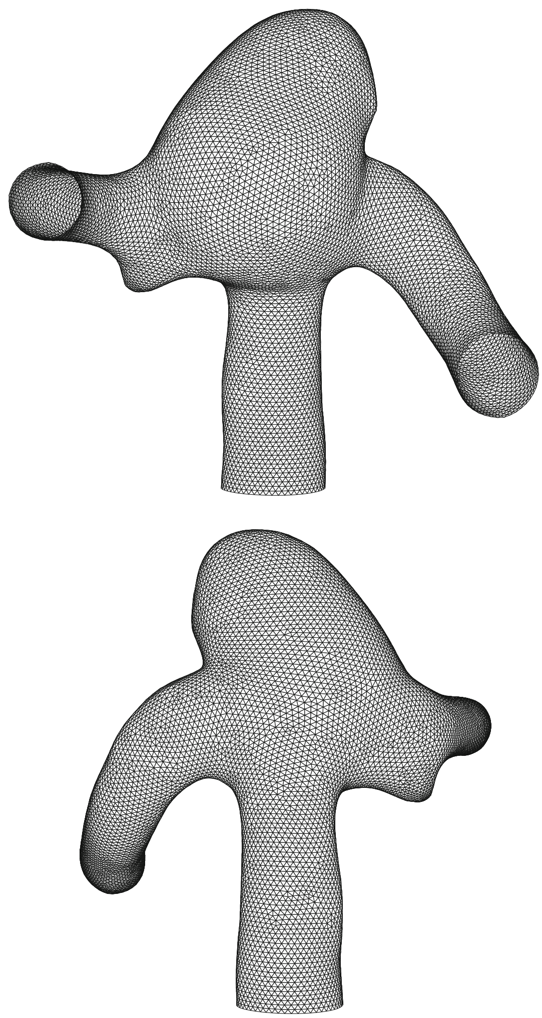

Fig. 8 A bifurcating middle cerebral artery segment with aneurysm. Fluid–structure interface for the fine fluid mechanics mesh

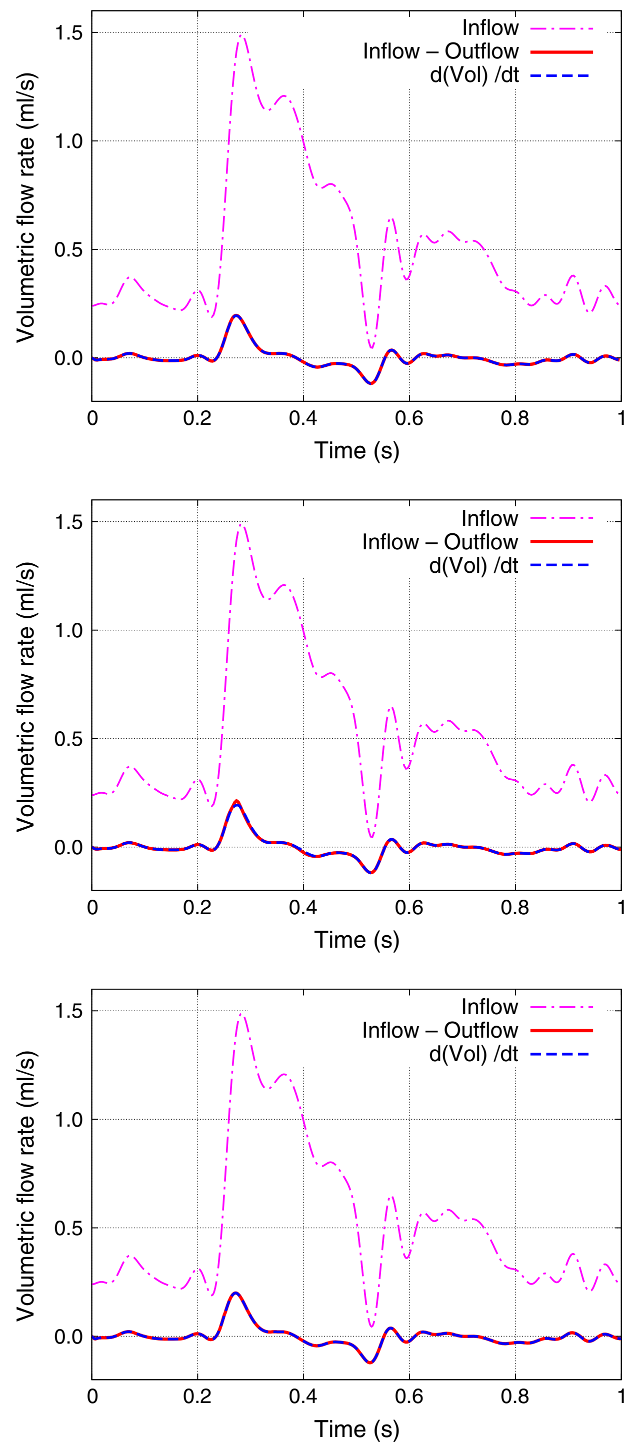

Fig. 9 A bifurcating middle cerebral artery segment with aneurysm. Verification of mass balance for the coarse (*top*), medium (*middle*) and fine (*bottom*) meshes. Volumetric inflow rate, difference between the volumetric inflow and outflow rates, and rate of change for the artery volume

function option WTSA (see Remark 1 in [9]). The stabilization parameters used are those given by Eqs. (12)–(18) in [9]. The damping coefficient η is set to 1.5×10^4 s^{-1}. The time-step size for coarse and medium meshes is 3.333×10^{-3} s and for fine mesh is 1.667×10^{-3} s. In the coarse and medium mesh computations, the number of nonlinear iterations per time step is 6, and the number of GMRES iterations per nonlinear iteration is 300 for the fluid and structural mechanics parts, and 30 for the mesh moving part. For all six nonlinear iterations the fluid scale is set to 1.0 and the structure scale to 50. In the fine mesh computations the number of GMRES iterations per nonlinear iteration is 600.

4.5 Results

We achieve good mass balance in all computations. This is verified by comparing the rate of change for the artery volume and the difference between the volumetric inflow and outflow rates. Figure 9 shows the mass balance for the coarse, medium and fine meshes. Figure 10 shows the WSS for the three meshes when the volumetric flow rate is maximum.

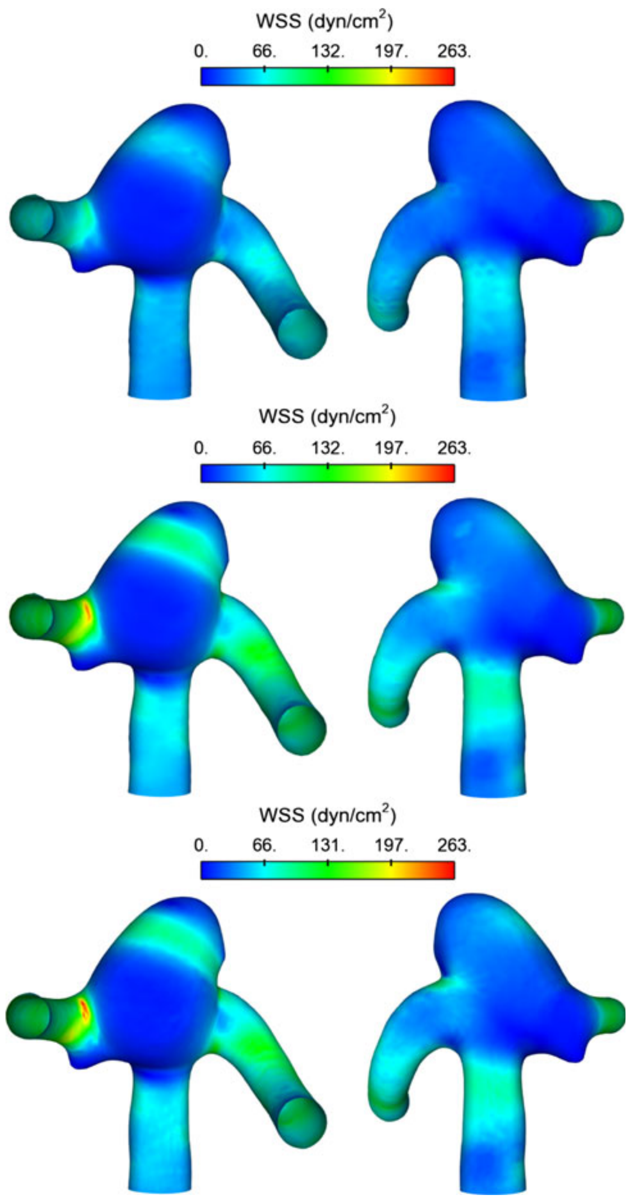

Fig. 10 A bifurcating middle cerebral artery segment with aneurysm. WSS for the coarse (*top*), medium (*middle*) and fine (*bottom*) meshes when the volumetric flow rate is maximum

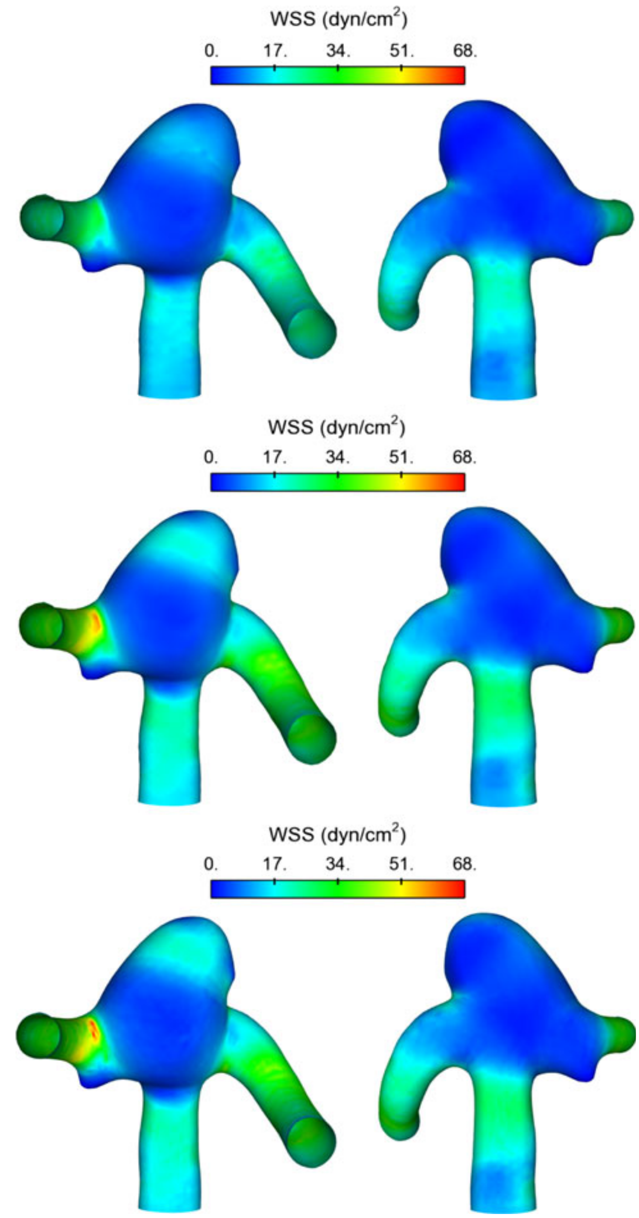

Fig. 11 A bifurcating middle cerebral artery segment with aneurysm. Time-averaged WSS for the coarse (*top*), medium (*middle*) and fine (*bottom*) meshes

Figure 11 shows the time-averaged WSS for the three meshes. Table 1 shows maximum, mean and minimum values of WSS for the three meshes.

Remark 6 Numbers shown in Table 1 are slightly different than the results reported in [16], and this is because we are calculating the WSS in a slightly different way.

Figure 12 shows the OSI for the three meshes. The higher OSI region indicates flow direction changes over the cardiac cycle. The medium and fine mesh results are in good agreement. Figure 13 shows typical streamlines around the higher OSI region. When the flow accelerates, a vortex forms, which

Table 1 A bifurcating middle cerebral artery segment with aneurysm

Mesh	Peak systole		Time average		
	Max	Mean	Max	Mean	Min
Coarse	102	37	32	12.53	0.16
Medium	237	54	60	16.76	0.32
Fine	263	53	68	16.53	0.24

WSS (dyn/cm^2) for the coarse, medium and fine meshes. Spatial maximum and mean at peak systole, and spatial maximum, mean and minimum of time-averaged values

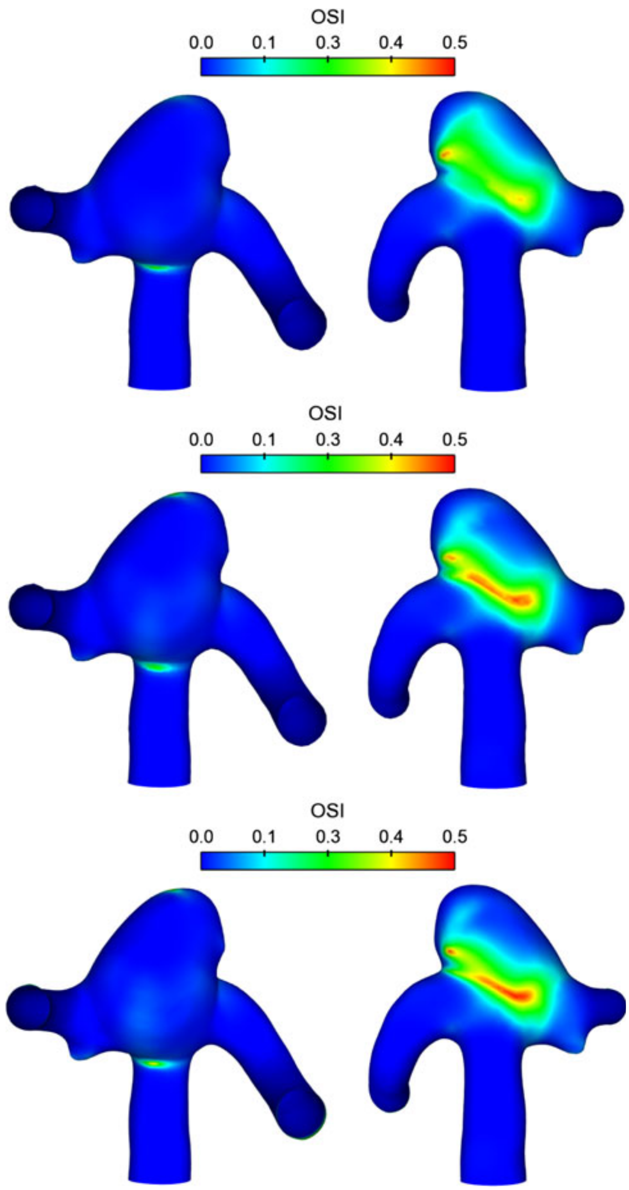

Fig. 12 A bifurcating middle cerebral artery segment with aneurysm. OSI for the coarse (*top*), medium (*middle*) and fine (*bottom*) meshes

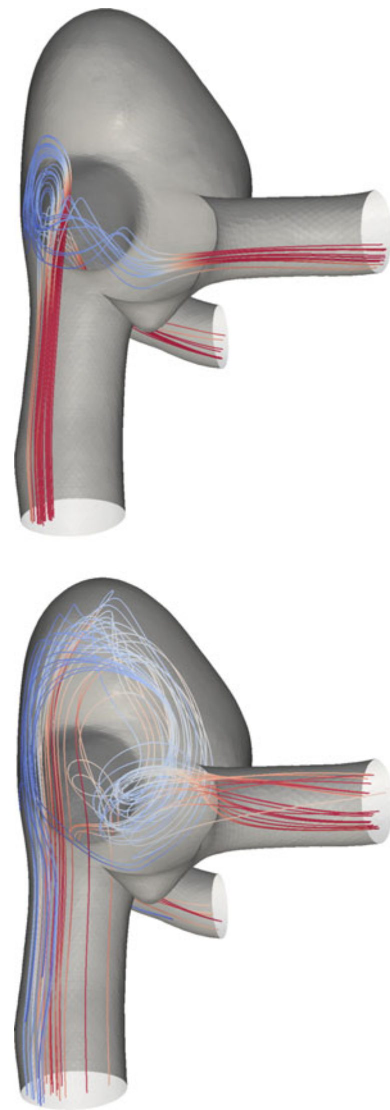

Fig. 13 A bifurcating middle cerebral artery segment with aneurysm. Streamlines computed with the fine mesh at the instants shown in Fig. 1: $t = 0.268$ s (*top*) and $t = 0.448$ s (*bottom*). The streamlines illustrate the WSS direction changes

results in a downward WSS. Conversely, when the flow decelerates, the vortex dissipates and the flow creates an upward WSS. One of the reasons behind this change in flow characteristics is the motion of the aneurysm. We observe an aneurysm movement towards the left in Fig. 13 when the flow accelerates.

5 Concluding remarks

We introduced special arterial FSI techniques for the projection of fluid–structure interface stresses, calculation of the wall shear stress (WSS), and calculation of the oscillatory shear index (OSI). The new stress projection technique makes the computations more efficient and the new way of calculating the WSS yields better results near the arterial ends. The OSI calculation technique we propose filters out the rigid-body rotation component that might otherwise enter into such calculations. We tested two different structural mechanics meshes and three different fluid mechanics meshes to investigate the influence of mesh refinement on the WSS calculations. Both structural mechanics meshes have the two layers of elements across the arterial wall, but different refinements along the wall. The fluid mechanics mesh refinements are both in the normal direction near the wall and on the wall. The test computations show that FSI plays an important role in WSS values and the fluid mechanics mesh with “medium” refinement provides reasonably good results.

Acknowledgments This work was supported in part by a Seed Grant from the Gulf Coast Center for Computational Cancer Research funded by John and Ann Doerr Fund for Computational Biomedicine. It was also supported in part by the Rice Computational Research Cluster funded by NSF under Grant CNS-0421109, and a partnership between Rice University, AMD and Cray. We are grateful to Dr. Ryo Torii (Imperial College) and Professor Marie Oshima (University of Tokyo) for providing the arterial geometry and inflow velocity data used in the computations.

References

1. Torii R, Oshima M, Kobayashi T, Takagi K, Tezduyar TE (2004) Influence of wall elasticity on image-based blood flow simulation. Jpn Soc Mech Eng J Ser A (in Japanese) 70:1224–1231
2. Gerbeau J-F, Vidrascu M, Frey P (2005) Fluid–structure interaction in blood flow on geometries based on medical images. Comput Struct 83:155–165
3. Torii R, Oshima M, Kobayashi T, Takagi K, Tezduyar TE (2006) Computer modeling of cardiovascular fluid–structure interactions with the deforming-spatial-domain/stabilized space–time formulation. Comput Methods Appl Mech Eng 195:1885–1895
4. Torii R, Oshima M, Kobayashi T, Takagi K, Tezduyar TE (2006) Fluid–structure interaction modeling of aneurysmal conditions with high and normal blood pressures. Comput Mech 38:482–490
5. Bazilevs Y, Calo VM, Zhang Y, Hughes TJR (2006) Isogeometric fluid–structure interaction analysis with applications to arterial blood flow. Comput Mech 38:310–322
6. Torii R, Oshima M, Kobayashi T, Takagi K, Tezduyar TE (2007) Influence of wall elasticity in patient-specific hemodynamic simulations. Comput Fluids 36:160–168
7. Tezduyar TE, Sathe S, Cragin T, Nanna B, Conklin BS, Pausewang J, Schwaab M (2007) Modeling of fluid–structure interactions with the space–time finite elements: arterial fluid mechanics. Int J Numer Methods Fluids 54:901–922
8. Torii R, Oshima M, Kobayashi T, Takagi K, Tezduyar TE (2007) Numerical investigation of the effect of hypertensive blood pressure on cerebral aneurysm—Dependence of the effect on the aneurysm shape. Int J Numer Methods Fluids 54:995–1009
9. Tezduyar TE, Sathe S, Schwaab M, Conklin BS (2008) Arterial fluid mechanics modeling with the stabilized space–time fluid–structure interaction technique. Int J Numer Methods Fluids 57:601–629
10. Bazilevs Y, Calo VM, Hughes TJR, Zhang Y (2008) Isogeometric fluid–structure interaction: theory, algorithms, and computations. Comput Mech 43:3–37
11. Torii R, Oshima M, Kobayashi T, Takagi K, Tezduyar TE (2008) Fluid–structure interaction modeling of a patient-specific cerebral aneurysm: Influence of structural modeling. Comput Mech 43:151–159
12. Isaksen JG, Bazilevs Y, Kvamsdal T, Zhang Y, Kaspersen JH, Waterloo K, Romner B, Ingebrigtsen T (2008) Determination of wall tension in cerebral artery aneurysms by numerical simulation. Stroke 39:3172–3178
13. Tezduyar TE, Schwaab M, Sathe S (2008) Sequentially-coupled arterial fluid–structure interaction (SCAFSI) technique. Comput Methods Appl Mech Eng, published online, doi:10.1016/j.cma.2008.05.024, July
14. Torii R, Oshima M, Kobayashi T, Takagi K, Tezduyar TE (2008) Fluid–structure interaction modeling of blood flow and cerebral aneurysm: Significance of artery and aneurysm shapes. Comput Methods Appl Mech Eng, published online, doi:10.1016/j.cma.2008.08.020, July
15. Bazilevs Y, Gohean JR, Hughes TJR, Moser RD, Zhang Y (2009) Patient-specific isogeometric fluid–structure interaction analysis of thoracic aortic blood flow due to implantation of the Jarvik 2000 left ventricular assist device. Comput Methods Appl Mech Eng, published online, doi:10.1016/j.cma.2009.04.015
16. Takizawa K, Christopher J, Tezduyar TE, Sathe S (2009) Space–time finite element computation of arterial fluid–structure interactions with patient-specific data. Commun Numer Methods Eng, published online, doi:10.1002/cnm.1241, March
17. Tezduyar TE, Takizawa K, Christopher J (2009) Multiscale sequentially-coupled arterial fluid–structure interaction (SCAFSI) technique. In: Hartmann S, Meister A, Schaefer M, Turek S (eds) International workshop on fluid–structure interaction—theory, numerics and applications. Kassel University Press, Kassel
18. Torii R, Oshima M, Kobayashi T, Takagi K, Tezduyar TE (2009) Influence of wall thickness on fluid–structure interaction computations of cerebral aneurysms. Commun Numer Methods Eng, published online, doi:10.1002/cnm.1289, July
19. Tezduyar T, Aliabadi S, Behr M, Johnson A, Mittal S (1993) Parallel finite-element computation of 3D flows. Computer 26:27–36
20. Tezduyar TE, Aliabadi SK, Behr M, Mittal S (1994) Massively parallel finite element simulation of compressible and incompressible flows. Comput Methods Appl Mech Eng 119:157–177
21. Mittal S, Tezduyar TE (1994) Massively parallel finite element computation of incompressible flows involving fluid–body interactions. Comput Methods Appl Mech Eng 112:253–282
22. Mittal S, Tezduyar TE (1995) Parallel finite element simulation of 3D incompressible flows—Fluid-structure interactions. Int J Numer Methods Fluids 21:933–953
23. Johnson AA, Tezduyar TE (1997) Parallel computation of incompressible flows with complex geometries. Int J Numer Methods Fluids 24:1321–1340
24. Johnson AA, Tezduyar TE (1999) Advanced mesh generation and update methods for 3D flow simulations. Comput Mech 23:130–143
25. Kalro V, Tezduyar TE (2000) A parallel 3D computational method for fluid–structure interactions in parachute systems. Comput Methods Appl Mech Eng 190:321–332
26. Stein K, Benney R, Kalro V, Tezduyar TE, Leonard J, Accorsi M (2000) Parachute fluid–structure interactions: 3-D Computation. Comput Methods Appl Mech Eng 190:373–386
27. Tezduyar T, Osawa Y (2001) Fluid–structure interactions of a parachute crossing the far wake of an aircraft. Comput Methods Appl Mech Eng 191:717–726
28. Ohayon R (2001) Reduced symmetric models for modal analysis of internal structural-acoustic and hydroelastic-sloshing systems. Comput Methods Appl Mech Eng 190:3009–3019
29. Stein K, Tezduyar T, Benney R (2003) Mesh moving techniques for fluid–structure interactions with large displacements. J Appl Mech 70:58–63
30. Tezduyar TE, Sathe S, Keedy R, Stein K (2004) Space–time techniques for finite element computation of flows with moving boundaries and interfaces. In: Gallegos S, Herrera I, Botello S, Zarate F, Ayala G (eds) Proceedings of the III international congress on numerical methods in engineering and applied science, CD-ROM, Monterrey, Mexico
31. Stein K, Tezduyar TE, Benney R (2004) Automatic mesh update with the solid-extension mesh moving technique. Comput Methods Appl Mech Eng 193:2019–2032
32. van Brummelen EH, de Borst R (2005) On the nonnormality of subiteration for a fluid–structure interaction problem. SIAM J Scientific Comput 27:599–621
33. Michler C, van Brummelen EH, de Borst R (2005) An interface Newton–Krylov solver for fluid–structure interaction. Int J Numer Methods Fluids 47:1189–1195

34. Tezduyar TE, Sathe S, Keedy R, Stein K (2006) Space–time finite element techniques for computation of fluid–structure interactions. Comput Methods Appl Mech Eng 195:2002–2027
35. Tezduyar TE, Sathe S, Stein K (2006) Solution techniques for the fully-discretized equations in computation of fluid–structure interactions with the space–time formulations. Comput Methods Appl Mech Eng 195:5743–5753
36. Tezduyar TE, Sathe S, Stein K, Aureli L (2006) Modeling of fluid–structure interactions with the space–time techniques. In: Bungartz H-J, Schafer M, (eds) Fluid–structure interaction. Lecture notes in computational science and engineering, vol 53. Springer, Berlin, pp 50–81
37. Dettmer W, Peric D (2006) A computational framework for fluid–structure interaction: finite element formulation and applications. Comput Methods Appl Mech Eng 195:5754–5779
38. Khurram RA, Masud A (2006) A multiscale/stabilized formulation of the incompressible Navier–Stokes equations for moving boundary flows and fluid–structure interaction. Comput Mech 38:403–416
39. Kuttler U, Forster C, Wall WA (2006) A solution for the incompressibility dilemma in partitioned fluid–structure interaction with pure Dirichlet fluid domains. Comput Mech 38:417–429
40. Lohner R, Cebral JR, Yang C, Baum JD, Mestreau EL, Soto O (2006) Extending the range of applicability of the loose coupling approach for FSI simulations. In: Bungartz H-J, Schafer M (eds) Fluid–structure interaction. Lecture notes in computational science and engineering, vol 53. Springer, Berlin, pp 82–100
41. Bletzinger K-U, Wuchner R, Kupzok A (2006) Algorithmic treatment of shells and free form-membranes in FSI. In: Bungartz H-J, Schafer M (eds) Fluid–structure interaction. Lecture Notes in Computational Science and Engineering, vol 53. Springer, Berlin, pp 336–355
42. Masud A, Bhanabhagvanwala M, Khurram RA (2007) An adaptive mesh rezoning scheme for moving boundary flows and fluid–structure interaction. Comput Fluids 36:77–91
43. Sawada T, Hisada T (2007) Fuid–structure interaction analysis of the two dimensional flag-in-wind problem by an interface tracking ALE finite element method. Comput Fluids 36:136–146
44. Wall WA, Genkinger S, Ramm E (2007) A strong coupling partitioned approach for fluid–structure interaction with free surfaces. Comput Fluids 36:169–183
45. Tezduyar TE, Sathe S (2007) Modeling of fluid–structure interactions with the space–time finite elements: solution techniques. Int J Numer Methods Fluids 54:855–900
46. Kuttler U, Wall WA (2008) Fixed-point fluid–structure interaction solvers with dynamic relaxation. Comput Mech 43:61–72
47. Dettmer WG, Peric D (2008) On the coupling between fluid flow and mesh motion in the modelling of fluid–structure interaction. Comput Mech 43:81–90
48. Tezduyar TE (1992) Stabilized finite element formulations for incompressible flow computations. Adv Appl Mech 28:1–44
49. Tezduyar TE, Behr M, Liou J (1992) A new strategy for finite element computations involving moving boundaries and interfaces—the deforming-spatial-domain/space–time procedure. I. The concept and the preliminary numerical tests. Comput Methods Appl Mech Eng 94:339–351
50. Tezduyar TE, Behr M, Mittal S, Liou J (1992) A new strategy for finite element computations involving moving boundaries and interfaces—the deforming-spatial-domain/space–time procedure: II. Computation of free-surface flows, two-liquid flows, and flows with drifting cylinders. Comput Methods Appl Mech Eng 94:353–371
51. Tezduyar TE (2003) Computation of moving boundaries and interfaces and stabilization parameters. Int J Numer Methods Fluids 43:555–575
52. Hughes TJR, Brooks AN (1979) A multi-dimensional upwind scheme with no crosswind diffusion. In: Hughes TJR (ed) Finite element methods for convection dominated flows, AMD-vol 34. ASME, New York, pp 19–35
53. Brooks AN, Hughes TJR (1982) Streamline upwind/Petrov–Galerkin formulations for convection dominated flows with particular emphasis on the incompressible Navier–Stokes equations. Comput Methods Appl Mech Eng 32:199–259
54. Tezduyar TE, Mittal S, Ray SE, Shih R (1992) Incompressible flow computations with stabilized bilinear and linear equal-order-interpolation velocity-pressure elements. Comput Methods Appl Mech Eng 95:221–242
55. Hughes TJR, Franca LP, Balestra M (1986) A new finite element formulation for computational fluid dynamics. V. Circumventing the Babuška–Brezzi condition: a stable Petrov–Galerkin formulation of the Stokes problem accommodating equal-order interpolations. Comput Methods Appl Mech Eng 59:85–99
56. Tezduyar TE, Behr M, Mittal S, Johnson AA (1992) Computation of unsteady incompressible flows with the finite element methods—space–time formulations, iterative strategies and massively parallel implementations. In: New methods in transient analysis, PVP-Vol 246/AMD-Vol 143. ASME, New York, pp 7–24
57. Johnson AA, Tezduyar TE (1994) Mesh update strategies in parallel finite element computations of flow problems with moving boundaries and interfaces. Comput Methods Appl Mech Eng 119:73–94
58. Tezduyar TE (2001) Finite element methods for flow problems with moving boundaries and interfaces. Arch Comput Methods Eng 8:83–130
59. Tezduyar TE (2004) Finite element methods for fluid dynamics with moving boundaries and interfaces. In: Stein E, De Borst R, Hughes TJR (eds) Encyclopedia of computational mechanics, vol 3: Fluids, Chap. 17. John Wiley & Sons, New York
60. Tezduyar TE, Cragin T, Sathe S, Nanna B (2007) FSI computations in arterial fluid mechanics with estimated zero-pressure arterial geometry. In: Onate E, Garcia J, Bergan P, Kvamsdal T (eds) Marine 2007, CIMNE, Barcelona, Spain
61. Tezduyar TE, Schwaab M, Sathe S (2007) Arterial fluid mechanics with the sequentially-coupled arterial FSI technique. In: Onate E, Papadrakakis M, Schrefler B (eds) Coupled Problems 2007, CIMNE, Barcelona, Spain
62. Saad Y, Schultz M (1986) GMRES: a generalized minimal residual algorithm for solving nonsymmetric linear systems. SIAM J Scientific Stat Comput 7:856–869
63. Tezduyar TE, Sathe S, Pausewang J, Schwaab M, Christopher J, Crabtree J (2008) Interface projection techniques for fluid–structure interaction modeling with moving-mesh methods. Comput Mech 43:39–49
64. Taylor CA, Hughes TJR, Zarins CK (1998) Finite element modeling of three-dimensional pulsatile flow in the abdominal aorta: relevance to atherosclerosis. Ann Biomed Eng 158:975–987
65. Green AE, Naghdi PM (1976) A derivation of equations for wave propagation in water of variable depth. J Fluid Mech 78:237–246
66. Huang H, Virmani R, Younis H, Burke AP, Kamm RD, Lee RT (2001) The impact of calcification on the biomechanical stability of atherosclerotic plaques. Circulation 103:1051–1056
67. Frank O (1899) Die grundform des arteriellen pulses. Zeitung fur Biologie 37:483–586
68. Bazilevs Y, Hsu M-C, Benson D, Sankaran S, Marsden A (2009) Computational fluid–structure interaction: methods and application to a total cavopulmonary connection. Comput Mech (accepted)